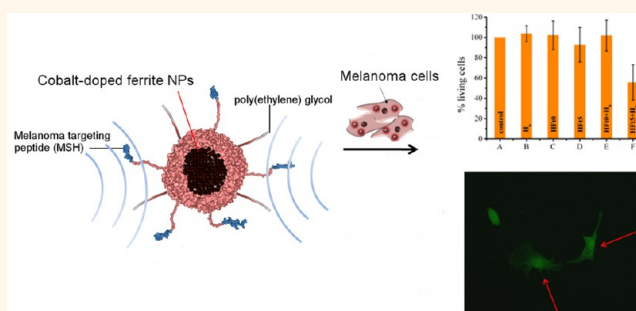# A Smart Platform for Hyperthermia Application in Cancer Treatment: Cobalt-Doped Ferrite Nanoparticles Mineralized in Human Ferritin Cages

Elvira Fantechi,[†] Claudia Innocenti,[†] Matteo Zanardelli,[‡] Maria Fittipaldi,[§] Elisabetta Falvo,[⊥] Miriam Carbo,[⊥] Valbona Shullani,[†] Lorenzo Di Cesare Mannelli,[‡] Carla Ghelardini,[‡] Anna Maria Ferretti,[∥,#] Alessandro Ponti,[∥,#] Claudio Sangregorio,[∥,†,▽,*] and Pierpaolo Ceci[⊥,*]

[†]INSTM and Dipartimento di Chimica "U. Schiff", Università degli Studi di Firenze, via della Lastruccia 3, I-50019 Sesto Fiorentino, Italy, [‡]Dipartimento di Neuroscienze, Psicologia, Area del Farmaco e Salute del Bambino - Sez. Farmacologia e Tossicologia, Università degli Studi di Firenze, Viale Pieraccini, 6 I-50139 Firenze, Italy, [§]INSTM and Dipartimento di Fisica e Astronomia, Università degli Studi di Firenze, via Sansone 1, I-50019 Sesto Fiorentino, Italy, [⊥]Istituto di Biologia e Patologia Molecolari, Consiglio Nazionale delle Ricerche, c/o Dip. Di Scienze Biochimiche, P.le Aldo Moro 5, I-00185 Roma, Italy, [∥]Istituto di Scienze e Tecnologie Molecolari, Consiglio Nazionale delle Ricerche, via C. Golgi 19, I-20133 Milano, Italy, and [#]Laboratorio di Nanotecnologie, Istituto di Scienze e Tecnologie Molecolari, Consiglio Nazionale delle Ricerche, via Fantoli 16/15, I-20138 Milano, Italy. [▽]Present address: Istituto di Chimica dei Composti Organo-Metallici, Consiglio Nazionale delle Ricerche, via Madonna del Piano 10, I-50019 Sesto Fiorentino, Italy.

ABSTRACT Magnetic nanoparticles, MNPs, mineralized within a human ferritin protein cage, HFt, can represent an appealing platform to realize smart therapeutic agents for cancer treatment by drug delivery and magnetic fluid hyperthermia, MFH. However, the constraint imposed by the inner diameter of the protein shell (*ca.* 8 nm) prevents its use as heat mediator in MFH when the MNPs comprise pure iron oxide. In this contribution, we demonstrate how this limitation can be overcome through the controlled doping of the core with small amount of Co(II). Highly monodisperse doped iron oxide NPs with average size of 7 nm are mineralized inside a genetically modified variant of HFt, carrying several copies of α-melanocyte-stimulating hormone peptide, which has already been demonstrated to have excellent targeting properties toward melanoma cells. HFt is also conjugated to poly(ethylene glycol) molecules to increase its *in vivo* stability. The investigation of hyperthermic properties of HFt-NPs shows that a Co doping of 5% is enough to strongly enhance the magnetic anisotropy and thus the hyperthermic efficiency with respect to the undoped sample. *In vitro* tests performed on B16 melanoma cell line demonstrate a strong reduction of the cell viability after treatment with Co doped HFt-NPs and exposure to the alternating magnetic field. Clear indications of an advanced stage of apoptotic process is also observed from immunocytochemistry analysis. The obtained data suggest this system represents a promising candidate for the development of a protein-based theranostic nanoplatform.

KEYWORDS: ferritin · magnetic nanoparticles · cobalt ferrite · magnetic fluid hyperthermia · cancer therapy

The interest in biocompatible multifunctional magnetic nanoparticles (MNPs) has grown exponentially in the past few years, and the enthusiasm is boosted by the many benefits envisaged by their introduction in clinical applications. In fact, MNPs are expected to strongly improve the performances of currently used diagnostic and therapeutic tools.[1,2] MNPs already entered the clinic market as contrast agents for magnetic resonance imaging (MRI), and clinical trials currently underway are demonstrating their efficacy as heat mediators in the magnetic fluid hyperthermia (MFH) treatment of glioblastoma, pancreas and prostate tumors.[3,4] However, several challenges remain to be faced to hold the many expectations raised. The most fascinating perspective is undoubtedly represented by the development of theranostic nanoplatforms, able to combine early diagnosis, monitoring, and tracking with multifold therapeutic treatments in the same single system. The keystone for the building up of such a novel

clinical approach is represented by a proper functionalization of the magnetic core that can ensure biocompatibility and endow specific targeting and delivery properties, meanwhile preserving good physical characteristics of the inorganic core to be employed in MRI and MFH.

Among the different functionalization strategies developed so far, the approaches using protein-cage structures, like those of the ferritin (Ft) family, are particularly promising.[5,6] Fts are ubiquitous proteins in nature, which are involved in iron homeostasis and storage. For biomedical applications, NPs based on the human Ft (HFt) present a number of favorable properties with respect to other systems. HFt is a physiological protein that has high solubility and stability in water, blood, and buffers, as well as low toxicity, all of which are desirable features for *in vivo* applications in human. Further, HFt can be easily functionalized through genetic engineering and/or chemical reactions involving one of the many chemical groups exposed to the exterior (primary amines, carboxylates, thiols)[7−10] granting the rational design of new nanometric tools for delivery,[11] imaging,[9,12,13] or therapy.[8,10,14−17] From a structural point of view, Fts are composed of 24 subunits self-assembled into a cage-like architecture surrounding an iron oxide core comprising up to *ca.* 4500 metal ions. The external diameter is 12 nm, and the size of the internal cavity is *ca.* 8 nm.[18,19] Since their biological function is iron sequestration and storage, they are natively tailored for iron uptake and NP incorporation, which may preclude the occasional release of toxic Fe(III) ions.[20] The exceptional stability of the Ft cage structure over a wide range of temperatures (up to 80−100 °C) and pH (3−10) makes large-scale production at low cost through recombination techniques possible. A wide choice of inorganic materials can be mineralized inside the apo form of Ft, which acts as a natural monodisperse and spherical-shaped template for the formation of inorganic NPs. NPs of Fe_3O_4,[21−26] Co_3O_4,[27,28] Mn_3O_4,[29] CoPt,[30] Pd,[31] Ag,[32] CdS,[33] CdSe,[34] and ZnSe[35] have been indeed synthesized within the Ft cage, with excellent homogeneity in terms of shape and size distribution.

However, the constraint to the growth of the inorganic nucleus imposed by the internal diameter of the Ft cavity represents an important limitation to their application in theranostic. In fact, while magnetite NPs with mean size equal to or lower than 8 nm can be effectively used in MRI application, they are too small for MFH trials. Theoretical and experimental studies have indeed demonstrated that the maximum MFH efficiency for magnetite NPs is reached for 15−18 nm in diameter and that it drops off sharply upon NP size decrease.[36−39]

A viable route to go beyond this limit is the increase of the magnetic anisotropy of the inorganic component, which can be simply realized through the total or partial replacement of ferrous ions with other, more anisotropic, divalent ions, the most prominent example being the introduction of cobalt ions. Indeed, it has been shown that cobalt ferrite NPs, whose magnetocrystalline anisotropy can be up to 20 times larger than that of magnetite, retain good heat dissipation property down to size of *ca.* 8 nm.[40] Interestingly, we investigated a family of Co-doped ferrite NPs with variable composition but identical size and found that the highest values of magnetic anisotropy are obtained with intermediate Co content.[41] This result suggests that better hyperthermic efficacy could be obtained using nonstoichiometric cobalt ferrite, with the additional advantage of keeping the toxicity level potentially introduced by the Co ions acceptably low.
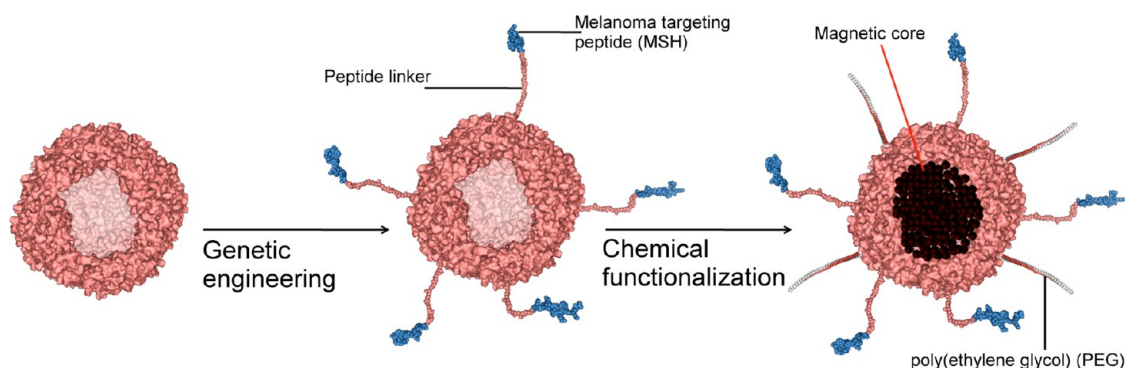
On the basis of these findings, we investigated the effect of doping ferrite NPs grown in HFt with an amount of Co lower than that required by $CoFe_2O_4$ stoichiometry, as a possible strategy to overcome the limit imposed by the size constraint, meanwhile fully exploiting the multiple advantages that Ft offers. In particular, we used a genetically modified variant of HFt (HFt-MSH) which carries at the N-terminal region of each subunit the α-melanocyte-stimulating hormone (α-MSH), a peptide that binds the melanocortin receptors selectively overexpressed by melanoma cells and metastases.[42] To avoid the nonspecific cell uptake of the HFt-NPs and ensure a satisfactory circulation time in the bloodstream, the surface of HFt-NPs was further conjugated with 5 kDa poly(ethylene glycol) (PEG) (Scheme 1).

Importantly, we have recently demonstrated that the HFt-MSH NPs are able to accumulate at the level of primary melanoma for extended periods of time (1−7 days), with high selectivity with respect to other organs.[43,44] Further, *in vivo* studies showed that HFt-MSH NPs are also able to target melanoma metastases, which represent the actual cause of melanoma mortality.

The structural and magnetic investigations carried-out in this work on Co-doped HFt-MSH NPs demonstrate that even a small amount of Co (5%) allows one to achieve a considerable hyperthermic effect, otherwise precluded using undoped iron oxide NPs. More importantly, the Co-doped construct was able to produce a hyperthermic effect on melanoma cells *in vitro*, causing a strong reduction of their viability. This result represents a significant step forward in the *in vivo* applications of Ft-based nanoplatform selectively targeted against melanoma.

RESULTS AND DISCUSSION

Synthesis and Structural Characterization. A set of four cobalt-doped magnetite NPs were prepared using a recombinant form of the HFt as bioreactor for the controlled synthesis of the NPs. Four different levels of doping, namely, 0, 5, 10, and 15% mol/mol with

Scheme 1. Schematic description of the HFt-based nanoplatform for melanoma targeting. The HFt protein has been genetically functionalized with α-MSH peptide, which was joined to the N-terminus of each of the 24 subunits by a peptide linker for targeted delivery (only 5 of the 24 derivatized N-termini are shown, for clarity). Subsequently, HFt has been chemically conjugated with PEG and filled with metal ions (Fe and Co) to obtain the magnetic core.
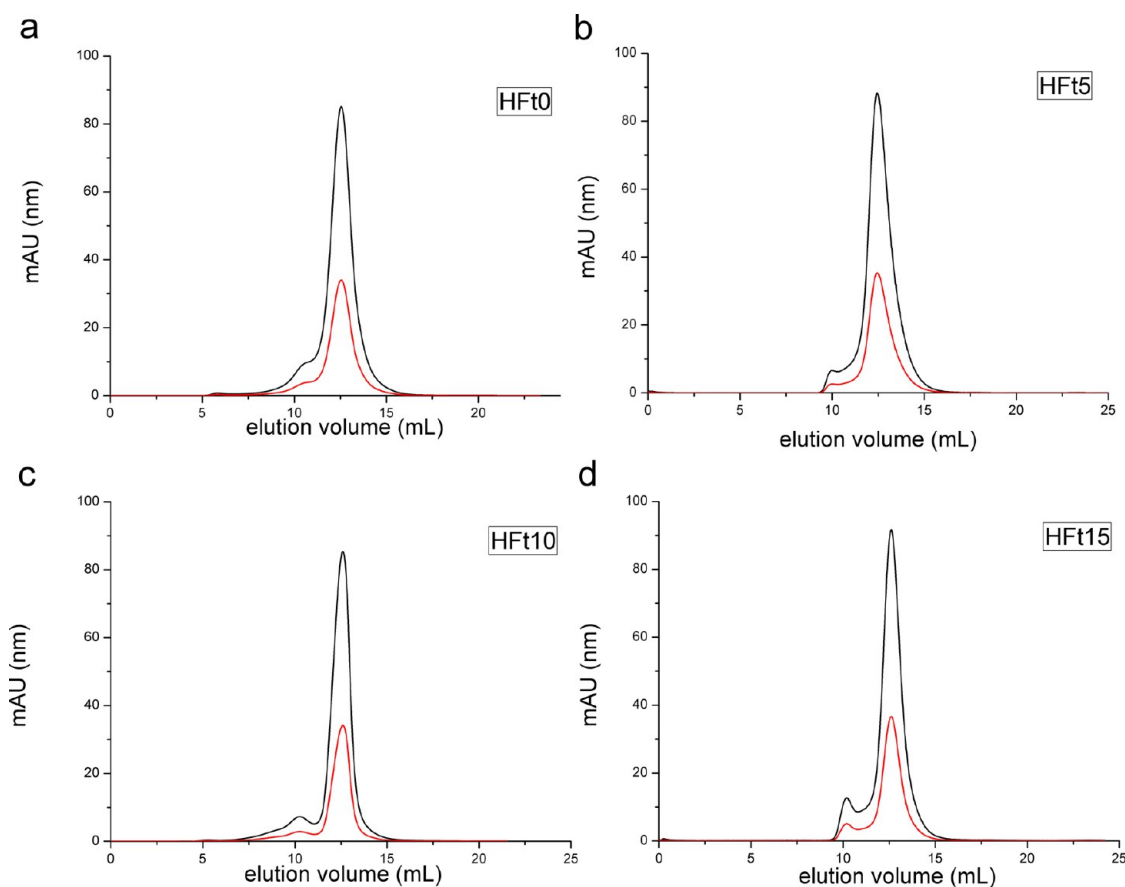

Figure 1. Gel-filtration elution profiles of Co-doped and undoped magnetite NPs mineralized in PEGylated HFt-MSH. Elution volumes of the four samples (HFt0, HFt5, HFt10 and HFt15) are almost identical, indicating that the overall morphology of the HFt cage is retained regardless of metal incorporation. Minor peaks eluting at ~10 mL represent an oligomeric state (mainly dimers) of the protein. Co-elution of the protein (black lines, 280 nm) and the metal cluster (red lines, 350 nm) indicates composite nature of HFt cage and metal particle.

respect to the total metal amount (labeled **HFt0**, **HFt5**, **HFt10**, and **HFt15**, respectively) were synthesized. The biomineralization reaction (details in Materials and Methods) was carried-out inside a PEGylated and genetically engineered form of HFt (HFt-MSH, Scheme 1), which carries the α-MSH peptide at the N-terminal end of each protein subunit and is able to selectively bind melanoma cells.[43] The Co-doped and undoped magnetite NPs obtained with HFt were first characterized by size exclusion gel filtration chromatography experiments to establish whether the NPs were effectively enclosed within the protein cage. After metal incorporation, all HFt samples elute like the apoprotein, indicating that the synthetic process does not significantly affect the overall protein structure and assembly. The elution pattern (Figure 1) shows coelution
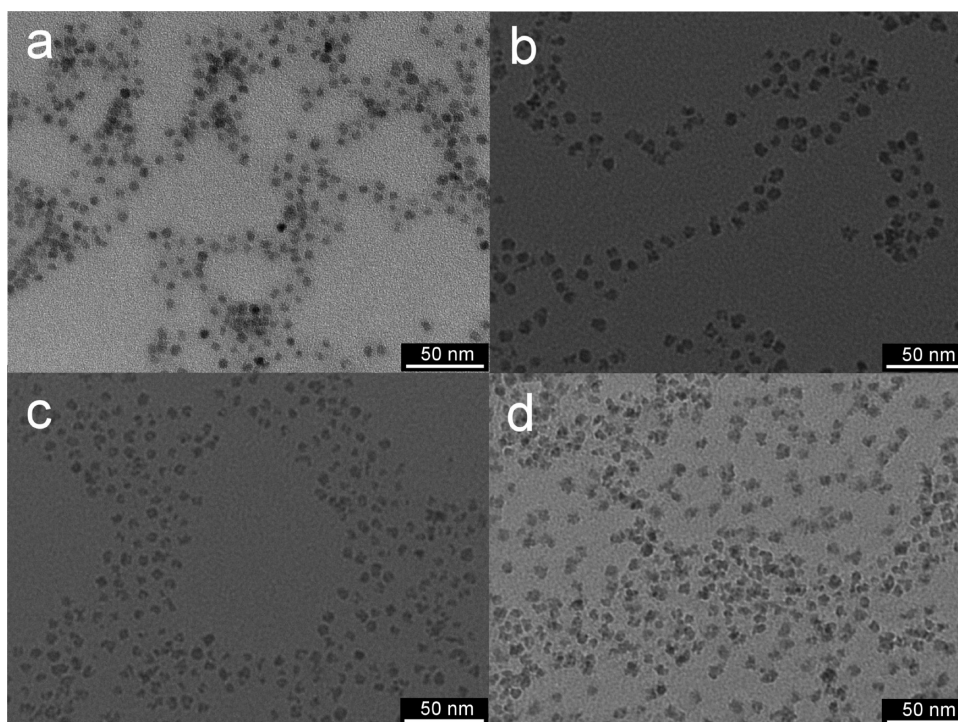
Figure 2. TEM images of HFt-NPs: (a) HFt0, $d_{mean} = 6.0 \pm 0.8$ nm; (b) HFt5, $d_{mean} = 6.8 \pm 1.3$ nm; (c) HFt10, $d_{mean} = 6.4 \pm 1.0$ nm and (d) HFt15, $d_{mean} = 6.8 \pm 1.0$ nm.

TABLE 1. Magnetic Properties of Co-Doped HFt-NPs Samples

	d_{mean} (nm)[a]	T_B (K)[b]	$\mu_0 H_c$ 2.5 K (mT)[c]	M_{5T} 2.5 K (Am²/kg)[d]	M_{5T} 300 K (Am²/kg)[e]	M_R[f]	M_{5T}/M_S[g]
HFt0	6.0 ± 0.8	20	44	88	75	0.40	0.94
HFt5	6.8 ± 1.3	149	880	120	96	0.71	0.96
HFt10	6.4 ± 1.0	150	1110	65	51	0.66	0.94
HFt15	6.8 ± 1.0	115	1320	43	28	0.44	0.84

[a] Average diameter and standard deviation obtained from the statistical analysis of TEM images. [b] Blocking temperature. [c] Coercive field at 2.5 K. [d,e] Magnetization at 5T (M_{5T}) normalized to the total metal content (Fe + Co) at low temperature (d) and at room temperature (e). [f] Reduced remanent magnetization (M_{0T}/M_{5T}). [g] Ratio of M_{5T} to the saturation magnetization (M_S), obtained by fitting the high-field data at room temperature to the relationship $M = M_S + a/H$. As a reference, the M_S per metal content at room temperature for bulk materials is 105, 110, and 126 Am²/kg for maghemite, cobalt ferrite, and magnetite, respectively.[66]

of the protein moiety (280 nm) and the ferrite cluster (350 nm), proving the composite nature of the material and indicating that practically all ferrite NPs are sequestered within the protein cage.

The cobalt to iron ratio of the NPs, determined by ICP-AES, resulted equal to the nominal one in all the doped samples, corresponding to formula unit Co$_x$Fe$_{3-x}$O$_4$ with x = 0, 0.15, 0.30, and 0.45 for **HFt0**, **HFt5**, **HFt10**, and **HFt15**, respectively.

The crystal structure of the obtained Co-doped NPs was investigated by powder X-ray diffraction. Due to the small size of the NPs and to the large amount of organic phase, the recorded diffractions patterns of HFt-NPs (Figure S1a in the Supporting Information) show an intense background and a low signal-to-noise ratio. In the diffraction patterns of **HFt0**, **HFt5**, and **HFt10**, all the peaks characteristic of the cubic crystalline phase of spinel oxides are observed, with a good match in both peak position and relative intensity

with the patterns of standard bulk cobalt ferrite (PDF-00-0221086), magnetite (PDF-00-019-0629) and maghemite (PDF-00-039-1346). Conversely, in the diffraction pattern of **HFt15**, only the two most intense peaks of cobalt ferrite are observed. The comparison among the most intense (311) peak of the different samples shows the increase of the width upon Co doping, suggesting a progressive decrease either of the physical crystallite diameter or of the sample crystallinity (Figure S1b in the Supporting Information). The lattice parameters, a, are 8.385(4), 8.382(1), 8.395(2), and 8.40(1) for **HFt0**, **HFt5**, **HFt10** and **HFt15**, respectively, in good agreement with those of bulk magnetite (8.3960 Å) and cobalt ferrite (8.3919 Å).

Unstained TEM of HFt samples (Figure 2) shows that all the samples are composed of irregularly shaped NPs with mean diameter ranging from 6.0 to 6.8 nm and narrow size distribution (see Table 1 and Figure S2 in the Supporting Information). The morphology of
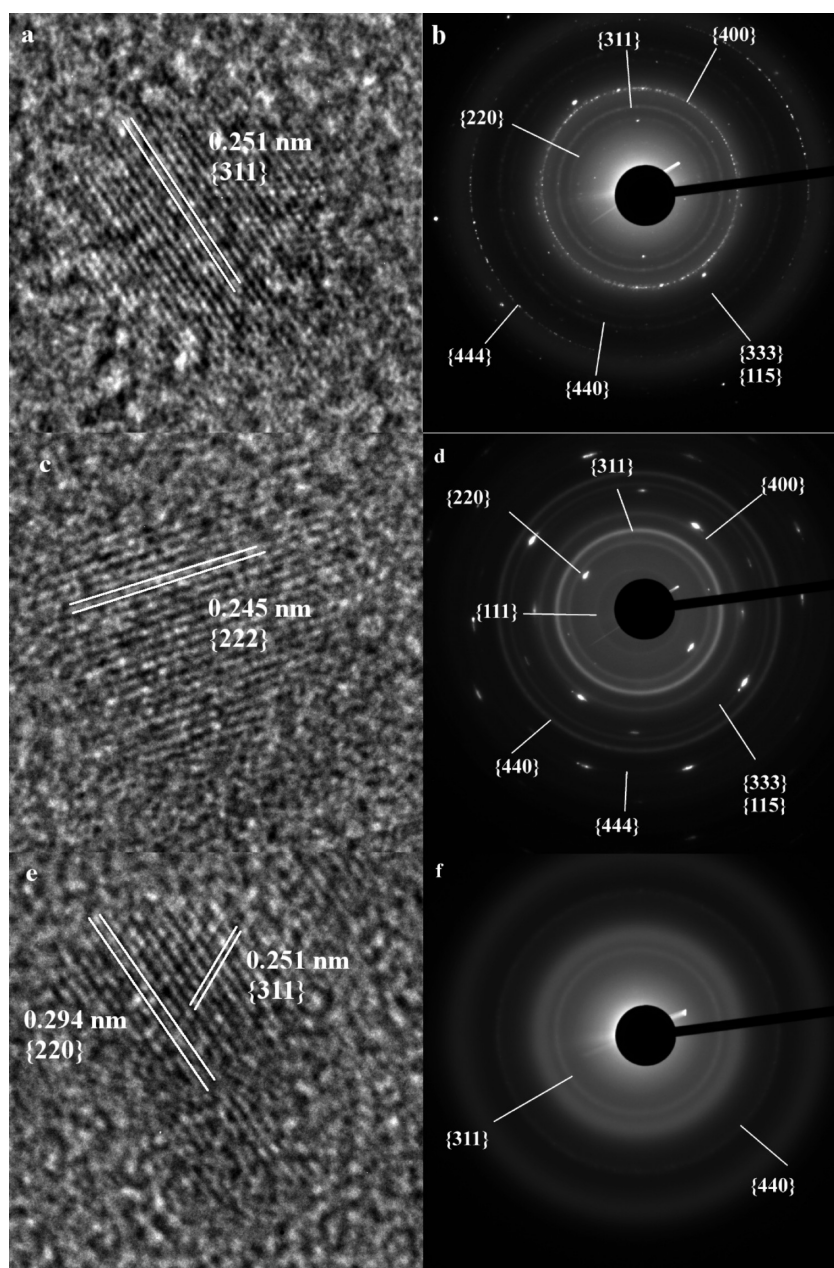
Figure 3. HR-TEM images and ED patterns of HFt5 (a and b), HFt10 (c and d) and HFt15 (e and f). In HR-TEM images (a, c, and e), lattices fringes are attributed to the corresponding crystal planes of the magnetite structure. In ED patterns (b, d, and f), diffraction rings are similarly labeled; the isolated diffraction spots in (b) and (d) are due to NaCl crystals from the PBS medium.

HFt-NPs becomes more irregular with increasing Co content, and **HFt15** shows a berry-like morphology.

To get further insight into the structural features of the HFt-NPs, high-resolution TEM (HR-TEM) images and electron diffraction (ED) patterns were recorded for the **HFt5**, **HFt10**, and **HFt15** samples (Figure 3). It should, however, be noted that, due to the similarity between Fe^{2+} and Co^{2+} ions, both techniques cannot discriminate between magnetite and cobalt-doped magnetite lattices. The fringe spacing corresponds to low-index planes of the magnetite structure. The ED patterns contain both powder-like diffraction rings and diffraction spots typical of single crystals (Figure 3b,d). The

spots correspond to low-index reflections of NaCl and can then be attributed to NaCl crystals formed by evaporation of the PBS buffer (see also Figure S1a in the Supporting Information). The diffraction rings correspond to low-index reflections of the magnetite structure in all samples ,but their relative intensity and width of the diffraction rings are significantly different. NPs in **HFt5** and **HFt10** give similar sets of diffraction rings, whereas only two diffraction rings (311) and (440) are observed in the ED pattern of **HFt15**. The shape of the (311) peaks (obtained by azimuthal averaging of the diffraction rings) are compared in Figure S3 in the Supporting Information.
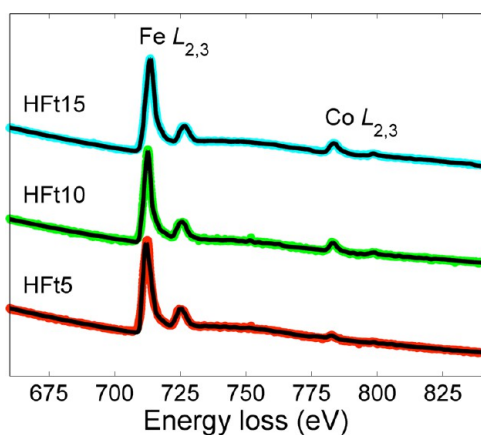
Figure 4. EELS spectra of samples HFt5 (red), HFt10 (green), and HFt15 (light blue). The spectra are normalized with respect to the Fe-L_3 peak intensity (712 eV) and offset for the sake of clarity. Best-fit spectra (black), obtained with the Co:Fe atomic ratio fixed to the ICP-AES value, are shown superimposed to the experimental spectra.

It is clear that the (311) peak has larger width in the **HFt15** sample (fwhm = 0.26 nm^{-1}) than in the **HFt5** and **HFt10** samples (fwhm = 0.20 nm^{-1}), consistently with the results obtained from XRD data analysis. These findings are evidence that, as the Co concentration increases, HFt-NPs are somehow less "crystalline", *i.e.*, some amorphous oxide is present or nanocrystals are smaller or more strained (or a combination of these effects).

To further investigate the chemical composition of the HFt-NPs, EELS spectra of the cobalt-containing HFt-NPs (Figure 4) were recorded. The Fe-$L_{2,3}$ edge (starting from 708 eV) and the Co-$L_{2,3}$ edge (starting from 779 eV) can be clearly seen. Note the decreasing intensity of the Co edge with decreasing Co content. To accurately measure the Co:Fe atomic ratio, we applied a best-fit procedure to the EELS spectra, as implemented in the EELS Model 3.3 software.[45] Unfortunately, it turned out that the problem is numerically not well-determined and statistically significant Co:Fe atomic ratios could not be obtained despite our efforts. We were therefore forced to limit ourselves to the question whether the EELS spectra are consistent with the Co:Fe atomic ratio obtained by the ICP-AES technique. We then applied the above best-fit procedure constraining the Co:Fe atomic ratio to the ICP-AES values. The constrained best-fit spectra, shown in Figure 4 as black lines, closely match the experimental ones showing that EELS results are consistent with ICP-AES data.

The distribution of the metal ions inside the cobalt containing HFt-NPs has been mapped using ESI, a TEM technique providing images of the distribution of specific chemical elements (see the Supporting Information). The Co (green) and Fe (red) elemental maps, together with a conventional TEM image as a reference, are collected in Figure 5. Making allowance for the unavoidable image shift due to nonsimultaneity

of the ESI experiments, one can see that there is a close match between the three images of each sample. This shows that each NP observed in conventional TEM mode contains both cobalt and iron, excluding the presence of NPs of pure iron or cobalt oxide. In agreement with ICP-AES and EELS results, Fe content is larger than Co content. Inspection of Figure 5 and of sections through selected HFt-NPs (Figure S4 in the Supporting Information) reveals that the Fe and Co elemental distributions in HFt-NPs are superimposed. There is thus no sign of chemical inhomogeneity within the HFt-NP volume, and the presence of cobalt oxide NPs in significant amount can be ruled out.

To investigate the presence of metal ions not incorporated into the inorganic core, electron paramagnetic resonance (EPR) spectra were recorded at variable temperature (5–240 K range) on **HFt5** as such and after dialysis over 40 h (sample **HFt5dial**). The spectra recorded at 240 K display a single asymmetric broad peak centered at $g = 2.23$ for both samples (Figure S5 in the Supporting Information). As the temperature is decreased, the resonance position moves toward lower field and the resonance broadens. This signal can be unambiguously attributed to the superparamagnetic resonance of the MNPs. Conversely, at low temperature, where the superparamagnetic resonance is so broad to be no more detectable, another broad signal, approximately 1000 G wide, around $g = 3.59$ appears in the spectrum of **HFt5**, which can be ascribed to paramagnetic Co^{2+} ions.[46] These ions can be either coordinated at the ferroxidase centers or at some of the many functional groups present at the surfaces of the ferritin moiety or, eventually, dissolved in the solution. In all cases the intensity of the signal is quite small, suggesting the number of Co ions not enclosed in the inorganic core is very low, of the order of few ‰ of the total cobalt amount (this approximately corresponds to one cobalt ion per ferritin construct). Importantly, the paramagnetic features completely disappeared after dialysis (Figure S5 in the Supporting Information).

Hyperthermic and Magnetic Characterization. The evaluation of hyperthermic efficiency was performed by recording the temperature kinetic curves of HFt-NPs colloidal solutions in PBS buffer exposed to an alternating magnetic field with parameters (12.4 kA/m amplitude and 183 kHz frequency) below the human tolerance threshold.[47] The total metal concentration in the samples was between 1.7 and 2.0% (w/w) of total metals. The kinetic curves, reported in Figure 6, show that the undoped sample, **HFt0,** does not produce a significant increase of temperature during the exposition to the alternating magnetic field, as indeed expected for magnetite NPs of this diameter.[36,38] Conversely, the presence of 5% of Co in the system causes a sizable increase of the temperature up to *ca.* 5 °C after 300 s of magnetic field application. For further
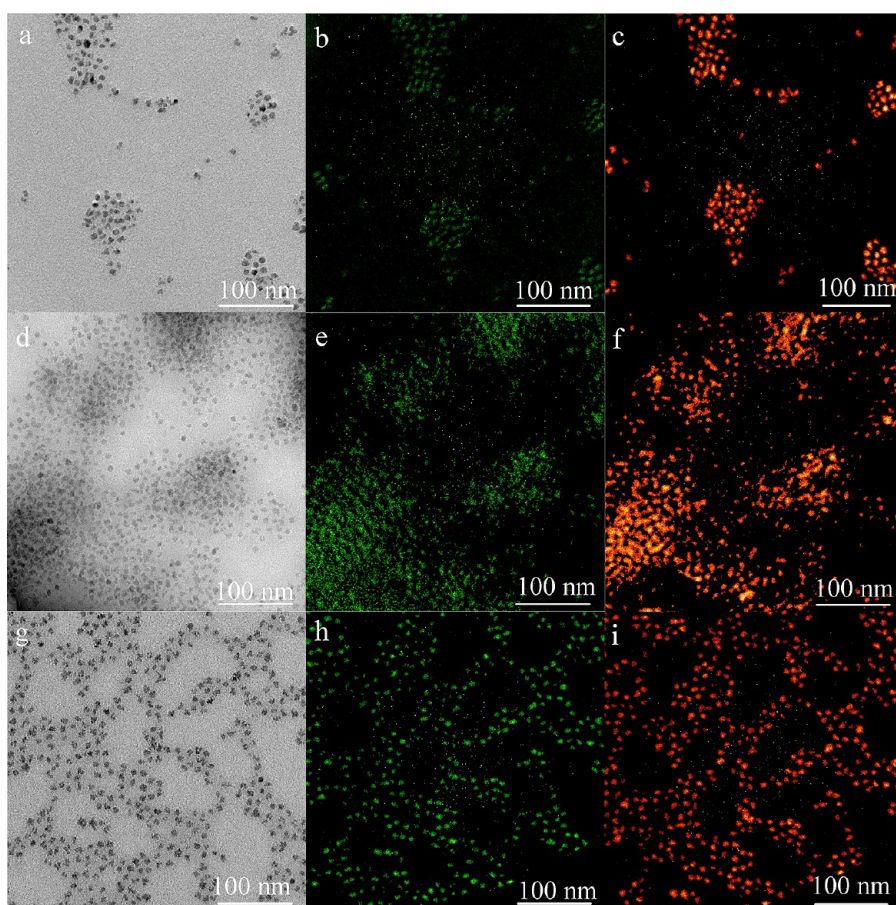
Figure 5. ESI elemental maps of HFt5 (a–c), HFt10 (d–f), and HFt15 (g–i). (a, d, and g) Conventional TEM image; (b, e, and h) ESI map at the Co-$L_{2,3}$ edge; (c, f, and i) ESI map at the Fe-$L_{2,3}$ edge. The elemental maps of each sample were collected using the same experimental setting.
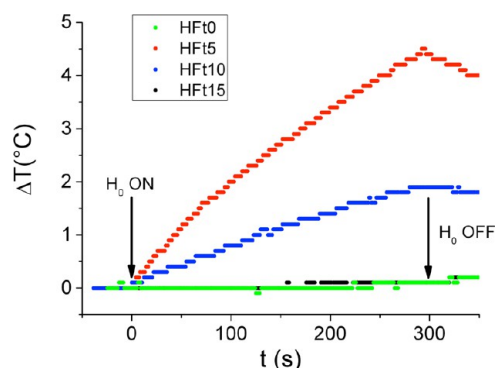

Figure 6. Temperature kinetics of samples HFt0 (2.0% w/w), HFt5 (1.8% w/w), HFt10 (1.7% w/w), and HFt15 (1.7% w/w) during the exposure to the alternating magnetic field (12.4 kA/m, 183 kHz). All measurements are performed starting from room temperature (21–22 °C).

increase of Co-doping, the temperature raise decreases, becoming almost zero for **HFt15**. The SAR values per mass of total metal ions (Co + Fe), evaluated from the initial slope of the kinetic curves, are 2.81 ± 0.02 and 1.3 ± 0.1 W/g for **HFt5** and **HFt10**, respectively. The obtained SAR values are very low if compared to data reported in the literature,[48–50] but we would like to underline that the size of the inorganic

core of our MNPs is much smaller than that of other nanosystems investigated to date; moreover, the external field parameters adopted in this experiment fall below the commonly admitted physiological tolerance threshold,[47] and can thus be transferred to clinical applications, while many other experiments use exceedingly high field amplitude and frequency, providing high, but therapeutically unserviceable, power losses.

A support to the rationalization of the observed hyperthermic behavior is provided by the investigation of the magnetic properties of the HFt-NPs. In Figure 7a, the ZFC and FC magnetization curves are reported; all HFt-NPs samples show the typical thermal irreversibility of an ensemble of single domain and weakly interacting MNPs, which can be described by the Néel-Brown model.[51] In this framework, the blocking temperature T_B, commonly identified with the temperature corresponding to the maximum of the ZFC curve, is directly proportional to the anisotropy barrier for the magnetic moment reversal, KV, where K is the magnetic anisotropy constant of the material and V is the average particle volume. The average T_B of HFt-NPs samples, reported in Table 1, are well below 250 K, indicating that all the samples are in the superparamagnetic regime at
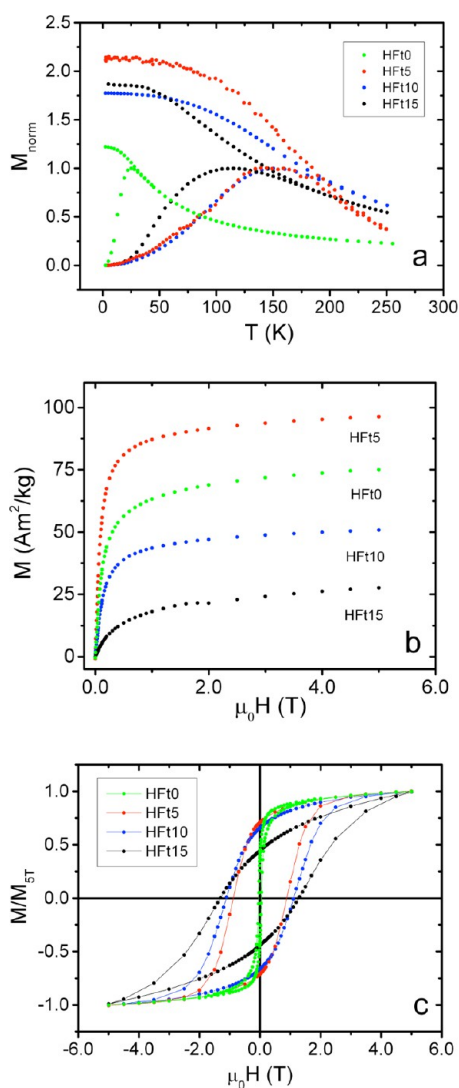
Figure 7. (a) Temperature dependence of the zero-field cooled (ZFC) and field-cooled (FC) magnetizations for HFt0, HFt5, HFt10, and HFt15, measured with a 5 mT probe field and normalized to the maximum of the ZFC curve; (b) room temperature M vs H curves; (c) hysteresis loops measured at 2.5 K, normalized to M_{5T}.

room temperature. The T_B value of **HFt0** (20 K) is consistent with that of maghemite/magnetite NPs of the same size reported in the literature.[52−54] A marked increase of T_B is observed when magnetite NPs are doped with 5% Co (T_B = 149 K for **HFt5**). This behavior is consistent with the substitution of the divalent iron ions with the much more anisotropic cobalt ones, which, increasing the magneto-crystalline anisotropy of the system, make the average blocking temperature higher. However, we did not observe the expected linear behavior on increasing the amount of Co, as T_B does not change on doubling the Co content (T_B = 150 K for **HFt10**), and even decreases to 115 K for **HFt15** (Table 1). A non-monotonous trend of magnetic anisotropy with Co content was already reported by us for 5−6 nm Co-doped maghemite NPs synthesized by thermal decomposition of metal-acetylacetonates. However, in that case,

the deviation from linearity was found above *ca.* 20% mol/mol of Co.[41]

In Figure 7b are reported the room temperature magnetization curves while the values of the magnetization at 5 T (expressed in Am^2/kg of total metal ions (Fe + Co)) are reported in Table 1. The saturation magnetization initially increases with Co doping, from 75 to 96 Am^2/kg for **HFt0** and **HFt5**, respectively, but it abruptly drops down on further increasing the doping level, being only 28 Am^2/kg for **HFt15**. Furthermore, the high field magnetization of the latter is more distant from saturation than the other samples (see M_{5T}/M_{sat} ratios reported in Table 1). A similar trend is exhibited by low temperature (2.5 K) hysteresis loops (Figures 7c and S6 in the Supporting Information): the shape of the loop becomes progressively less squared and less saturated, and, for **HFt15** is not closed up to the highest measuring field. Moreover, while the coercive field increases with the Co content, the remnant magnetization, $M_R = M_{0T}/M_{5T}$, decreases from **HFt5** to **HFt15** (Table 1). The M_R values of 0.40 and 0.44, recorded for **HFt0** and **HFt15**, respectively, are slightly lower than the typical one (0.5) expected for a set of isolated uniaxial NPs whose easy axis are isotropically oriented. On the other hand, the M_R values for **HFt5** and **HFt10** (0.71 and 0.66, respectively), evidence the dominant contribution of the cubic magneto-crystalline term, characteristic of crystalline ferrite (the expected value for a pure cubic system is 0.83).[55] Conversely, uniaxial anisotropy is generally assumed for small sized nanosystems, where the large surface to volume ratio favors the symmetry breaking occurring at the surface.

The observed magnetic behavior of HFt-NPs is consistent with the progressive loss of crystallinity evidenced by both X-ray and electron diffraction experiments. Indeed, if on one hand, increasing the amount of cobalt makes the magneto-crystalline anisotropy larger, on the other, the crystalline disorder lowers the spin alignment thus reducing the effective magnetic volume (lower T_B) and the remnant and saturation magnetizations, increasing the coercivity ($\mu_0 H_C$) and modifying the approach to saturation. In any case, the strong increase of the magnetic anisotropy observed in the nanosystem enables us to rule out the concomitant formation, even in the form of a thin shell layer, of a Co-rich antiferromagnetic secondary phase, such as Co_3O_4, as observed by Klem *et al.*[56] in an attempt of mineralizing cobalt ferrite nanoparticles within ferritin cages. This result is further supported by ESI analysis.

The above interpretation is corroborated by the comparison of the low temperature cycles recorded after a ZFC procedure with those obtained after field cooling the sample from room temperature with a 5 T magnetic field. While the ZFC and FC loops of **HFt5** and **HFt10** overlap, for sample in **HFt15** the loop clearly shifts toward negative fields (Figure S7 in the
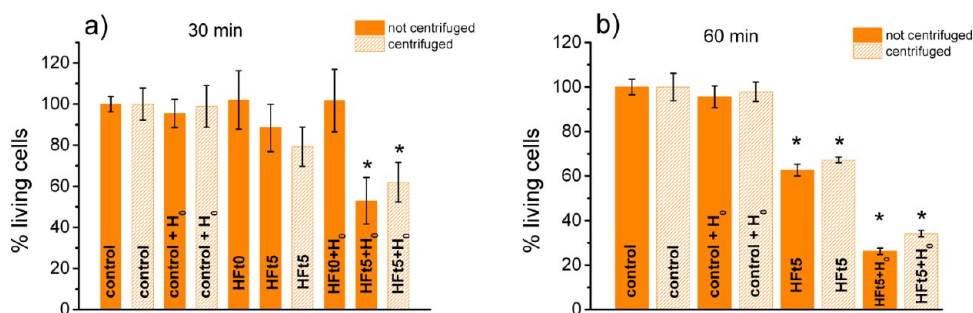
Figure 8. Evaluation of the hyperthermic efficacy of HFt-NPs on melanoma B16 cell viability using MTT assay. Melanoma cells were incubated for (a) 30 or (b) 60 min at room temperature with a of 0.3% (w/w) HFt-NPs solution, applying (labeled as HFt0 + H_0 and HFt5 + H_0) or not (labeled as HFt0 and HFt5) an alternating magnetic field of amplitude H_0 = 17.0 kA/m and frequency f = 183 kHz for 30 min. Cell suspensions were measured as such (full bars) or after centrifuge at 1400 rpm for 10 min to separate cells from the unbound NPs (dashed bars). Control samples without and with application of the magnetic field (labeled control and control + H_0, respectively) are also reported in the graphs. Results are expressed in percentage as mean ± SEM of 4 experiments. Control condition was fixed to 100%. *P < 0.05 *vs* control.

Supporting Information) by 27.5 mT, while the coercivity is increased by 8 mT. This behavior is the typical signature of exchange bias, a very complex phenomenon which is generally observed in system where an interface between different magnetic phases occurs, including classical exchange coupled antiferro/ferro(i) magnetic systems, combination of ferro-, canted antiferro-, and spin-glass magnetic components.[57,58] Nevertheless, a shift of the FC loop has been also reported for structurally single phase metal oxide nanostructures, where the bias is generated at the interface between frozen spin glass- like disordered and the magnetically ordered regions, as indeed observed in our case.[59]

The magnetic properties can explain the trend observed in the calorimetric experiments. Indeed, in the linear regime the power loss is proportional to the frequency, f, to the square amplitude, H_0, of the magnetic field and to the out-of-phase component of the magnetic susceptibility, χ'':

$$SAR \propto f\mu_0 H_0^2 \chi''$$

χ'' increases with the magnetic moment of the NPs, and depends nonlinearly on f, reaching a maximum when the magnetic moment reversal time above the energy barrier, τ_N, matches the period of the applied field. Within our series, this latter condition is better satisfied by samples with higher T_B. Therefore, since the spoiling of crystallinity reduces both M_S and T_B, it cuts down the heat dissipation capability of the NPs, nullifying the effect of a large Co doping.

In Vitro Hyperthermic Efficiency Tests on B16 Melanoma Cell Line. The sample with the highest SAR (**HFt5**) was selected to test *in vitro* the hyperthermic efficiency of the nanosystem on a mouse melanoma B16 cell line and the obtained data were compared to those of the undoped sample (**HFt0**), which, according to SAR experiments described above, should have no thermal effect on cancer cell. Cells were incubated with a solution of HFt-NPs (0.3% w/w of total metal ions) for

30 or 60 min and then exposed for 30 min to an alternating magnetic field of 17.0 kA/m and 183 kHz. Alternatively, prior to the magnetic field exposure, cell suspensions were centrifuged to separate them from the unbound or weakly bound HFt-NPs. The effect of the different compounds and conditions was evaluated by measuring the cell viability with respect to a control sample through the MTT assay performed 48 h after treatments. The effect of the magnetic field alone was also evaluated by exposing untreated cells to the magnetic field following the same protocol applied to the treated sample. Moreover, to test the possible toxicity induced by Co-doping, the MTT test was performed after incubating cells with the same concentration (0.3% w/w of total metal ions) of **HFt5** and **HFt0**, without applying the oscillating magnetic field.

The obtained results, shown in Figure 8, clearly indicate that the application of the field to the cell culture incubated with **HFt5** NPs causes a significant reduction in cell viability. The extent of this viability reduction depends on the incubation time, with a greater effect at 60 min incubation (~70% of mortality, Figure 8b) with respect to the 30 min incubation (~45%, Figure 8a). Importantly, the large mortality found cannot be ascribed only to the potential toxicity of Co ions included in the inorganic lattice, since a significant smaller effect (10−30%), which presumably can be attributed to the small amount of Co ions present at the exterior of the protein cage, was observed on cells incubated with **HFt5** without the application of the magnetic field (Figure 8). Notably, no effect was observed when the same treatment is applied on cells incubated with the undoped **HFt0** (Figure 8a). Similar results were obtained measuring the number of live cells by Trypan blue assay and the number of cell colonies by DAPI nuclear staining (not shown). On the other hand, the possibility that the reduction in cell viability may arise from Co release induced by the alternating field application rather than
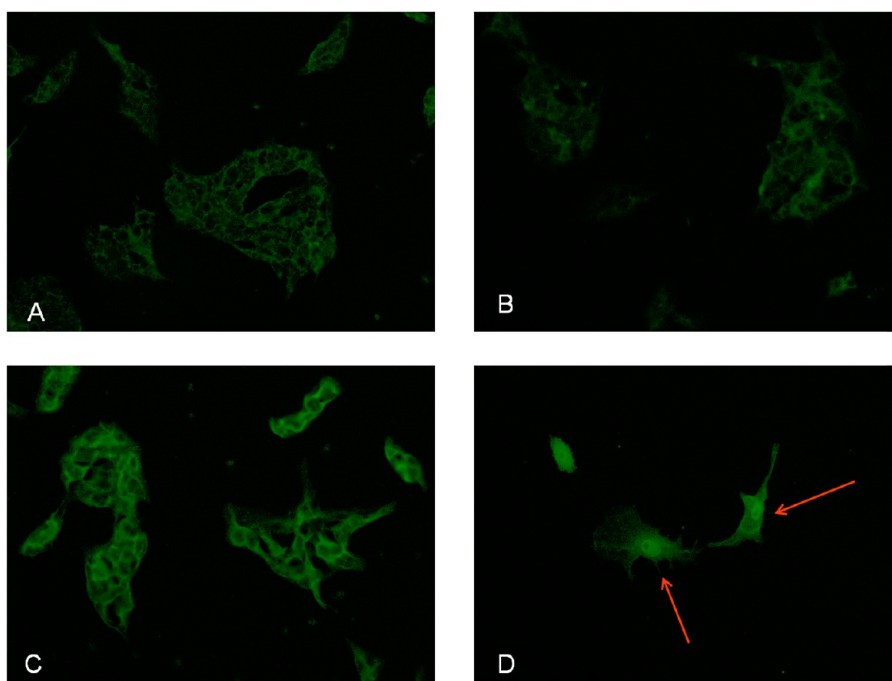
Figure 9. Immunofluorescence staining of the apoptotic enzyme caspase-3 in B16 cells. (A) control sample; (B) cells exposed to the magnetic field; (C) cells + HFt5; (D) cells + HFt5 exposed to the magnetic field. The alternating magnetic field of amplitude H_0 = 17.0 kA/m and frequency f = 183 kHz was applied for 30 min.

from a thermal effect, can be discarded. Indeed, in the EPR spectra of **HFt5dial**, after the application of the same alternating field, no signals arising from paramagnetic metal ions are observed, while the peak attributed to the superparamagnetic resonance of the metal oxide core, observed at 240 K, is not modified by the field application (Figure S5 in the Supporting Information).

Finally, it is important to remark that no significant differences in cell viability were observed when the experiment was repeated on cell culture after removal of unbound HFt-NPs by centrifugation. In fact, as shown in Figure 8, less than a 5% difference was observed. These results indicate that (i) most of HFt-NPs present in the cell suspension are strongly bound and/or internalized by cancer cells, in accordance with our previous report describing the high targeting ability against melanoma cells possessed by this selective nanoconstruct,[43,44] and (ii) HFt-NPs selectively exert their toxic effects after binding and/or internalization.

To gain insight into the cell death process induced by the field application, an immunocytochemistry investigation was performed to evaluate the caspase-3 expression. Caspase-3 is a hallmark of apoptotic cell death since this enzyme is a central effector of both intrinsic and extrinsic apoptosis pathways.[60] The percentage of fluorescence intensity normalized to the control sample is reported as Supporting Information (Figure S8). The apoptotic process is evoked by the treatment with **HFt5** alone or in combination with the alternating magnetic field. Nevertheless, the morphological analysis (Figure 9) reveals a characteristic increase of caspase-3 in the cell nucleus only in the sample treated with **HFt5** and exposed to the field with respect to the sample treated with **HFt5** alone. Although the precursor form of caspase-3 is localized in the cytoplasm, caspase-3 plays essential roles in nuclear changes of apoptotic cells.[61] In fact, caspase-3 translocates from the cytoplasm into the nucleus only during the apoptosis phenomenon by diffusion through the disrupted nuclear-cytoplasmic barrier and by an active transport system.[62] Hence, the presence of caspase-3 at the nuclear level strongly suggests a higher progression of the apoptotic process in cells treated with **HFt5** and exposed to magnetic fields with respect to the cells treated with **HFt5** alone.

These results demonstrate that also NPs with size below 8 nm can have a significant effect on tumor cell viability, provided their magnetic anisotropy is largely increased, a goal that, in the present case, has been achieved through the doping with the high anisotropy Co ions. However, the amount of doping required to trigger the cell death was found to be small. The latter aspect is crucial in view of a possible clinical application of HFt-MSH-NP in melanoma treatment, since it means that the biocompatibility of the nanoplatform is preserved in spite of the presence of toxic Co^{2+} ions, as indeed demonstrated by cell viability assays. Further, the possibility of conjugating additional drugs on the HFt external surface should allow further reducing the required therapeutic HFt-NPs dose, making this system

very appealing for future bimodal treatments based on hyperthermia and chemotherapy. This case is of special interest since a synergistic effect when heat and drugs are combined has been shown for several drugs, including the potential to reverse chemoresistance.[63]

It is also worth to stress that we obtained a significant reduction of cell viability although the nanosystem exhibits a very low SAR value if compared to commonly reported systems in the literature.[48−50] Different sources may concur to determine this result. A first explanation can be found in the excellent targeting efficiency of the **HFt5** NPs. In fact, recently we demonstrated that the **HFt0** NPs are able to largely accumulate inside the melanoma cells *in vitro*, and at the level of primary melanoma and lung metastases *in vivo* in a tumor-bearing mouse model.[43,44] Further, NPs accumulation occurred for extended periods of time (up to 7 days) and with high selectivity with respect to other organs,[44] suggesting that HFt-based constructs may be exploited to deliver high concentration of heat mediators to melanoma cells *in vivo* while reducing possible toxic side effects. A large bioaccumulation of the HFt construct in proximity or inside the melanoma cells could be then responsible for heat release *in situ*, starting the apoptotic process once the alternating magnetic field is applied, and preserving the healthy tissues which are not reached by the NPs. A second property which must be recalled to explain the *in vitro* efficacy of the HFt-Co construct despite of its low SAR is that the temperature at the surface of the NPs can be several tenths of degrees higher than the average increase measured in the calorimetric experiment. The presence of a strong temperature gradient, which is foreseen by all the models for MFH,[64] has been recently verified by the temperature evaluation in close proximity of the surface of iron oxide NPs exposed to an ac magnetic field, exploiting thermolabile PEGylated ligands.[65] Therefore, it can be argued that, although the total warming of cancerous cells remains low, the intracellular delivery of nanometric hot spots is enough to induce the onset of the apoptotic process. Finally, we wish to note that our result is not unprecedented since a similar result was recently reported by Villanueva *et al.*,[66] who observed apoptotic cell death of HeLa tumor cells incubated with silica coated $La_{0.56}(SrCa)_{0.22}MnO_3$ NPs, although the temperature increase in the cell culture was lower than 0.5 °C.

CONCLUSIONS

We have demonstrated that HFt-MSH can offer a viable platform for designing a smart therapeutic agent for treatment of melanoma provided the magnetic core mineralized within the apoferritin comprises a small amount of a high anisotropic ion. To summarize, Co-doped magnetite were mineralized within a PEGylated human variant of apo-ferritin

(HFt), genetically engineered in order to carry a targeting peptide for melanoma, α-MSH. Three different Co-doping levels were investigated and compared with the behavior of the undoped sample. The mineralization reaction gives NPs with a spherical morphology, a mean diameter slightly lower than the size of internal cavity (6−7 nm) and a narrow size distribution. For small amount of Co (5% mol/mol), the doping was found to improve the hyperthermic efficacy, as it increases the magnetic anisotropy of the material. However, a further increase of the doping level is detrimental for hyperthermic performance since it affects the crystal quality of the NPs. This trend could be related to the fact that several components are acting together during the mineralization process occurring in the ferritin cage system, *i.e.*: (i) the electrostatic gradients present along the pore channels traversing the protein shell, and (ii) the specific metal affinity to the catalytic (ferroxidase) and nucleation sites present inside the protein cage. This condition is substantially different from that operating during the common used chemical synthesis methods where all the ions freely diffuse and are available at once. The validation of this hypothesis is the subject of a specific structural study currently in progress.

The therapeutic potential of **HFt5** was tested *in vitro* on melanoma B16 cell lines. The application of an alternating magnetic field below the physiological tolerance limit for 30 min has shown to halve the vitality of cells treated with a **HFt5** solution (0.3% w/w of total metal ions), while the same procedure performed on cells incubated with undoped HFt-NPs had no effect. The marking of caspase-3, an enzyme characteristic of the apoptotic process, provided clear indication of an advanced stage of the apoptotic process in melanoma cells treated with **HFt5** and exposed to the magnetic field. The capability of the nanoconstruct to accumulate at intracellular level granted by its high targeting efficacy toward melanoma cells causes a satisfactory reduction of cell viability in spite of the low temperature increase produced by the magnetic seeds, as observed in the calorimetric measurements. However, for the size range imposed by the protein shell of ferritins, the Co doping appears as a mandatory requirement in order to deliver the minimal amount of energy to make the apoptotic process efficient.

Importantly, Co-doped HFt-MSH-NPs represents an example of an extremely small functionalized targeting nanosystem exploitable for MFH. Both the use of a targeted physiological protein and the reduction of the total size of therapeutic carrier are of paramount importance for *in vivo* applications, allowing for a selective cellular uptake, meanwhile reducing the risk of associated side effects. Finally, our result suggests that a different approach, which tries to take into account the system as a whole rather than focusing

on a single physical functionality, should be pursued to realize efficient antitumoral agents. Moreover, the possibility of further functionalizing the nanoconstruct with chemotherapeutic agents may open the way toward a multimodal approach in which NP-mediated heat release can amplify the cytotoxic drug action.

MATERIALS AND METHODS

Preparation of HFt-NPs. All procedures required to obtain HFt-MSH, namely, cloning, overexpression, and purification of HFt genetically linked to α-MSH, and subsequent conjugation of exposed cysteine residues with 5 kDa PEG was performed as previously described.[43]

The doped and undoped HFt-NPs were prepared at 65 °C at 1 mg/mL protein concentration in 5 mM HEPES-NaOH (Sigma-Aldrich, Italy) pH of 8.5. Solutions of iron(II) sulfate heptahydrate (Sigma-Aldrich, Italy), dissolved in 0.5 mM HCl were used as an iron source. For Co doped samples, cobalt(II) sulfate heptahydrate (Sigma-Aldrich, Italy) was added to the iron salt and dissolved in 0.5 mM HCl. The initial total metal concentration of the solutions used was 15 mM (for example, for **HFt5** the iron and cobalt concentrations were 14.25 and 0.75 mM, respectively). During the synthesis, the reaction vessel was kept at 65 °C under a positive N_2 pressure and the pH was maintained dynamically at 8.5 with 100 mM NaOH by means of an automatic titrator (TITRANDO, Metrohm AG). Solutions of $FeSO_4$/$CoSO_4$ (15 mM) and H_2O_2 (5 mM) were added simultaneously at a constant rate of 0.5 mL/min using two automatic titrators of the TITRANDO system (software TIAMO). Any aggregate of protein or metal oxides produced outside the protein cavity during NPs formation was removed by centrifugation at 16 000 rpm for 45 min at 4 °C followed by filtration through 0.2 μm filters. Then the NP solutions were ultrafiltrated and washed 3 times with phosphate buffered saline (PBS) by using 100 kDa Amicon Ultra-15 centrifugal filter devices (Millipore Corporate) to remove excess reagents. The HFt samples were sterile filtered and stored at 4 °C. Then, samples were checked by using a Superose 6 gel-filtration column (GE Healthcare) equilibrated with PBS. All NP samples had a loading factor of about 3600 metal atoms/protein molecule as assessed by native electrophoresis on 1% agarose gels.

The Co/Fe metal ratio was evaluated by inductively coupled plasma–atomic emission spectroscopy (Varian 720-ES ICP-AE Spectrometer; measurements performed on diluted samples after digestion in concentrated nitric acid) and found nearly identical to the nominal values.

Transmission Electron Microscopy (TEM). Average diameter and size distribution of HFt-NPs were determined from TEM images recorded using a CM12 PHILIPS transmission electron microscope operating at 100 kV. Samples were prepared by drop drying a dilute solution of HFt-NPs in PBS buffer onto 200 mesh carbon-coated copper grids. The recorded micrographs were further analyzed with the Image Pro-Plus software. The mean diameter and size distribution of each sample were obtained from a statistical analysis over 500–600 NPs.

High-resolution TEM (HR-TEM), electron diffraction (ED), electron energy loss spectroscopy (EELS), and electron spectroscopic imaging (ESI) of HFt-NPs were carried out using a Zeiss LIBRA 200FE-HR TEM, operating at 200 kV and equipped with an in-column omega filter for energy selective imaging and diffraction. Both HR-TEM and ED data have been collected using only elastically scattered electrons. EELS spectra were collected exciting a sample area of about 10 μm² and using the following microscope setting: illumination angle 250 μrad, collection angle ~6.7 mrad, spectral magnification 31.5k. EELS spectra were fitted to a theoretical model using the EELSModel 3.3 program.[45] The model used hydrogenic L-edge cross sections based on SIGMAL2[67] and included the fine structure of the Fe-$L_{2,3}$ and Co-$L_{2,3}$ edges[68] and plural scattering, *via* convolution of the model with the experimental zero-loss peak. Elemental maps of Co and Fe were obtained by ESI at the corresponding $L_{2,3}$ edge using the following microscope setting: energy window 12 eV (**HFt5** and **HFt15**) or 10 eV (**HFt10**), illumination

angle 1 mrad, collection angle ~13 mrad. The background was subtracted by the three-window white-line method. Images were processed by means of the iTEM TEM Imaging Platform software (Olympus).

XRD Diffraction Measurement. Powder X-ray diffraction (XRD) measurements were carried out using a Bruker New D8 Advance diffractometer equipped with Cu Kα radiation and fast multichannel high-resolution energy-dispersive 1-D detector, operating in $\theta-2\theta$ Bragg–Brentano geometry at 40 kV and 40 mA.

EPR Characterization. EPR spectra at X-band (9.39 GHz) were recorded by using a Bruker Elexsys E500 spectrometer equipped with a continuous-flow ^{4}He cryostat (ESR 900, Oxford Instruments). Spectra were acquired on dispersions in PBS buffer using a field modulation of 100 kHz and 9 G. A microwave power of 2 μW was used to record the spectra at 240 K and of 2 mW for those at 5 K.

Magnetic Characterization. Magnetic measurements were performed using a Quantum Design MPMS SQUID magnetometer operating in the 1.8–350 K temperature range and with an applied field up to 5 T. Measurements were performed on HFt-NPs dispersions in PBS buffer. All data were corrected for the diamagnetic contribution of the sample holder. Zero Field Cooled-Field Cooled (ZFC/FC) curves were obtained by measuring the temperature dependence of the magnetization applying a probe magnetic field (5 mT), after cooling the sample in the presence (FC) or in the absence (ZFC) of the field. The temperature was limited to 250 K in order to avoid the melting of the solvent during the temperature scan. The accuracy of H_C, M_R and M_S evaluation can be estimated as low as 1%. A rough estimate of T_B value accuracy is given by the half interval between the temperatures of two subsequent acquisition points, *i.e.*, 2.5 K.

Specific Absorption Rate (SAR) Measurements. The determination of SAR was performed through calorimetric measurements, by recording temperature kinetics of HFt-NPs exposed to an alternating magnetic field. Measurements were performed adapting a commercial setup, composed by a 6 kW Fives Celes power supply, a water-cooled induction coil and a series of variable capacitors (420 nF to 4.8 μF) for setting the required frequency. Such resonant RLC circuit is able to produce an alternating magnetic field in the range of 50–400 kHz and with amplitude up to 19.1 kA/m. The frequency and field amplitude values used in this work (183 kHz, 12.4/17.0 kA/m) were chosen in order to operate under the physiological limit, $H \cdot \nu < 5 \times 10^9$ A m^{-1} s^{-1}, beyond which deleterious responses of living tissues are observed.[40] The sample was placed in the middle of the induction coil, inside a polystyrene sample holder placed in a glass Dewar, in order to preserve the system form thermal gradients of the coil and the surroundings. The real amplitude of the magnetic field is determined by a AMF Life Systems high frequency probe. Measurements of the sample temperature were performed by an optical fiber thermometer connected to a digital temperature recorder (Fotemp).

The SAR values were calculated using the equation SAR = $(\Sigma_i m_i c_{pi}/m_{Me})(\Delta T/\Delta t)$, where ΔT is the temperature increase in the interval of time Δt, m_{Me} is the total mass of metal, m_i is the mass in grams of the i-species and C_{pi} is their specific heat. The sum is extended to all the i species involved in the heat exchange. Since the measurements are carried in non adiabatic conditions, the $\Delta T/\Delta t$ values were extrapolated for $t \rightarrow 0$ from temperature kinetic curves, by considering the initial slope.

***In Vitro* Hyperthermic Efficiency Tests on B16 Melanoma Cell Lines.** *Cell Cultures.* The murine B16 melanoma cells were obtained from the American Type Culture Collection (Rockville, MD). Cells were cultured in high glucose Dulbecco's modified Eagle's medium (DMEM) supplemented with 10% fetal bovine serum

(FBS; Gibco, Invitrogen, Italy) in a 5% CO_2 atmosphere at 37 °C. Medium contained 2 mM L-glutamine, 100 IU mL^{-1} penicillin, and 100 μg mL^{-1} streptomycin (Sigma, Germany). Cells were trypsinized with Tripsin-EDTA solution 1× for 5 min and then neutralized with culture medium. A total of 2 × 10^5 cells were suspended in 200 μL of DMEM plus 0.375% carboxymethyl cellulose (CMC) to favor a homogeneous suspension and incubated for 30 or 60 min at room temperature in the presence or in the absence of 0.3% (w/w) HFt-NPs. An oscillating magnetic field of 17.0 kA/m and 183 kHz was applied to the cell suspension for 30 min unless otherwise specified. Alternatively, cell suspensions were centrifuged at 1400g for 10 min to separate cells from the unbound NPs. Then cell pellets were resuspended in 200 μL of DMEM plus 0.375% CMC and subjected to the oscillating magnetic field. For this purpose, cell samples were placed in the middle of the induction coil, inside a glass container thermostatized by circulating ethylene glycol, in order to keep the system at 37 °C and to avoid thermal gradients of the coil and the surroundings. After the exposure to the magnetic field, cells were incubated at room temperature for 20 min. Cells were washed twice in PBS 1× and suspended in 200 μL of culture medium. A volume of 40 μL of the cells suspension was used to perform Trypan Blue assay. Twenty microliters of the cells suspension was plated on L-polylisinated glass, and the sample was incubated in 5% CO_2 atmosphere at 37 °C and, after 48 h, was used for immunocytochemistry experiments. Thirty microliters of the cells suspension was plated into 96 well culture plates and the sample was incubated in 5% CO_2 atmosphere at 37 °C; 48 h after, MTT assay was performed.

Trypan Blue Assay. B16 cells were diluted with 0.4% trypan blue (Sigma-Aldrich, Italy), pipetted onto a Burker chamber and counted under a microscope at 40× magnification. Live cells excluded the dye, whereas dead cells admitted the dye and consequently stained intensely with trypan blue. The number of viable cells for each experimental condition was counted.

MTT Assay. Cell viability was evaluated by the reduction of 3-(4,5-dimethylthiozol-2-yl)-2,5-diphenyltetrazolium bromide (MTT; Sigma-Aldrich, Italy). A total of 1 mg/mL of MTT was added into each well and the samples were incubated for 30 min at 37 °C. After washing, the formazan crystals were dissolved in 100 μL of dimethyl sulfoxide. The absorbance was measured at 550 nm.

Immunocytochemistry. Cell cultures were fixed at room temperature for 25 min with 4% paraformaldehyde in PBS. Cells were washed twice and subsequently incubated for 30 min at room temperature with a solution of Bovine Serum Albumin (BSA) 1% in PBS, before exposure to the rabbit anti-Caspase-3 antibodies (Cell Signaling) diluted in the same BSA solution. The primary antibody was diluted 1:100 and it detects endogenous levels of full length caspase-3 and the large fragment of caspase-3 resulting from cleavage. After an overnight incubation at 4 °C, cells were rinsed three times for 10 min in PBS and then incubated (1 h, room temperature) with secondary goat anti-rabbit antibodies conjugated to Alexa Fluor 488 (Invitrogen, Italy; 1:500 in PBS). Subsequently, nuclei were labeled with the fluorescent dye Hoechst 33258 (1:1000 in PBS, Invitrogen, Italy). Cells were rinsed three times in PBS. Coverslips were mounted with ProLong Gold Antifade Reagent (Invitrogen, Italy) and analyzed using a fluorescence microscope (Zeiss) connected to a computer equipped with Zeiss image software. Nonspecific staining was evaluated on sections where the primary antibody was omitted from the staining procedure.

Cell Colony Count. Cells nuclei were labeled with Hoechst reagent, as described above. Image were taken with the same fluorescent microscope used for immunocytochemistry experiments. A single cell colony was considered for cell group >10.

Statistical Analysis. Results were expressed as means ± SEM and the variance analysis was performed by ANOVA. A Bonferroni's significant difference procedure was used as post-hoc comparison. P-values of less than 0.05 were considered significant.

Supporting Information Available: Powder X-ray diffraction pattern of HFt-NPs; histograms of HFt-NPs size obtained from low-resolution TEM micrographs; comparison of the (311) peaks observed in the ED patterns of the Co-doped samples; section of the Fe and Co elemental distributions across selected nanoparticles; EPR spectra of **HFt5** and **HFt5dial**; hysteresis loops at 2.5 K of the Co-doped samples after ZFC and FC procedures; expression levels of the apoptotic enzyme caspase-3 in B16 cells. This material is available free of charge *via* the Internet at http://pubs.acs.org.

REFERENCES AND NOTES

1. Colombo, M.; Carregal-Romero, S.; Casula, M. F.; Gutiérrez, L.; Morales, M. P.; Böhm, I. B.; Heverhagen, J. T.; Prosperi, D.; Parak, W. J. Biological Applications of Magnetic Nanoparticles. *Chem. Soc. Rev.* **2012**, *41*, 4306–4334.

2. Special Issue: Theranostic Nanomedicine *Acc. Chem. Res.* **2011**, *44*, 841–1134.

3. Johannsen, M.; Gneveckow, U.; Taymoorian, K.; Thiesen, B.; Waldöfner, N.; Scholz, R.; Jung, K.; Jordan, A.; Wust, P.; Loening, S. A. Morbidity and Quality of Life During Thermotherapy Using Magnetic Nanoparticles in Locally Recurrent Prostate Cancer: Results of a Prospective Phase I Trial. *Int. J. Hyperthermia* **2007**, *23*, 315–323.

4. Maier-Hauff, K.; Ulrich, F.; Nestler, D.; Niehoff, H.; Wust, P.; Thiesen, B.; Orawa, H.; Budach, V.; Jordan, A. Efficacy and Safety of Intratumoral Thermotherapy Using Magnetic Iron-Oxide Nanoparticles Combined with External Beam Radiotherapy on Patients with Recurrent Glioblastoma Multiforme. *J. Neurooncol.* **2011**, *103*, 317–324.

5. Bode, S. A.; Minten, I. J.; Nolte, R. J.; Cornelissen, J. J. Reactions Inside Nano Scale Protein Cages. *Nanoscale* **2011**, *3*, 2376–2389.

6. Heddle, J. G. Protein Cages, Rings and Tubes: Useful Components of Future Nanodevices? *Nanotechnol., Sci. Appl.* **2008**, *1*, 67–78.

7. Falvo, E.; Tremante, E.; Fraioli, R.; Leonetti, C.; Zamparelli, C.; Boffi, A.; Morea, V.; Ceci, P.; Giacomini, P. Antibody-Drug Conjugates: Targeting Melanoma with Cisplatin Encapsulated in Protein-Cage Nanoparticles Based on Human Ferritin. *Nanoscale* **2013**, *5*, 12278–12285.

8. Kang, H. J.; Kang, Y. J.; Lee, Y. M.; Shin, H. H.; Chung, S. J.; Kang, S. Developing an Antibody-Binding Protein Cage as a Molecular Recognition Drug Modular Nanoplatform. *Biomaterials* **2012**, *33*, 5423–5430.

9. Lin, X.; Xie, J.; Niu, G.; Zhang, F.; Gao, H.; Yang, M.; Quan, Q.; Aronova, M. A.; Zhang, G.; Lee, S.; *et al.* Chimeric Ferritin Nanocages for Multiple Function Loading and Multimodal Imaging. *Nano Lett.* **2011**, *11*, 814–819.

10. Li, X.; Qiu, L. H.; Zhu, P.; Tao, X. Y.; Imanaka, T.; Zhao, J.; Huang, Y. G.; Tu, Y. P.; Cao, X. N. Epidermal Growth Factor-Ferritin H-Chain Protein Nanoparticles for Tumor Active Targeting. *Small* **2012**, *8*, 2505–2514.

11. Uchida, M.; Flenniken, M. L.; Allen, M.; Willits, D. A.; Crowley, B. E.; Brumfield, S.; Willis, A. F.; Jackiw, L.; Jutila, M.; Young, M. J.; *et al.* Targeting of Cancer Cells with Ferrimagnetic Ferritin Cage Nanoparticles. *J. Am. Chem. Soc.* **2006**, *128*, 16626–16633.

12. Valero, E.; Tambalo, S.; Marzola, P.; Ortega-Muñoz, M.; López-Jaramillo, F. J.; Santoyo-González, F.; de Dios López, J.; Delgado, J. J.; Calvino, J. J.; Cuesta, R.; *et al.* Magnetic Nanoparticles-Templated Assembly of Protein Subunits: A New Platform for Carbohydrate-Based MRI Nanoprobes. *J. Am. Chem. Soc.* **2011**, *133*, 4889–4895.

ARTICLE

13. Makino, A.; Harada, H.; Okada, T.; Kimura, H.; Amano, H.; Saji, H.; Hiraoka, M.; Kimura, S. Effective Encapsulation of a New Cationic Gadolinium Chelate Into Apoferritin and its Evaluation as an MRI Contrast Agent. *Nanomedicine* **2011**, *7*, 638–646.

14. Uchida, M.; Willits, D. A.; Muller, K.; Willis, A. F.; Jackiw, L.; Jutila, M.; Young, M. J.; Porter, A. E.; Douglas, T. Intracellular Distribution of Macrophage Targeting Ferritin−Iron Oxide Nanocomposite. *Adv. Mater.* **2009**, *21*, 458–462.

15. Fan, K.; Cao, C.; Pan, Y.; Lu, D.; Yang, D.; Feng, J.; Song, L.; Liang, M.; Yan, X. Magnetoferritin Nanoparticles for Targeting and Visualizing Tumour Tissues. *Nat. Nanotechnol.* **2012**, *7*, 459–464. Erratum in: 833.

16. Dominguez-Vera, J. M.; Fernandez, B.; Galvez, N. Native and Synthetic Ferritins for Nanobiomedical Applications: Recent Advances and New Perspectives. *Future Med. Chem.* **2010**, *2*, 609–618.

17. Li, K.; Zhang, Z. P.; Luo, M.; Yu, X.; Han, Y.; Wei, H. P.; Cui, Z. Q.; Zhang, X. E. Multifunctional Ferritin Cage Nanostructures for Fluorescence and MR Imaging of Tumor Cells. *Nanoscale* **2012**, *4*, 188–193.

18. Chiancone, E.; Ceci, P.; Ilari, A.; Ribacchi, V.; Stefanini, S. Iron and Proteins for Iron Storage and Detoxification. *Biometals* **2004**, *17*, 197–202.

19. Watt, R. K. The Many Faces of the Octahedral Ferritin Protein. *Biometals* **2011**, *24*, 489–500.

20. Theil, E. C. Ferritin Protein Nanocages Use Ion Channels, Catalytic Sites, and Nucleation Channels to Manage Iron/Oxygen Chemistry. *Curr. Opin. Chem. Biol.* **2011**, *15*, 304–311.

21. Bulte, J. W. M.; Douglas, T.; Mann, S.; Frankel, R.; Moskowitz, B. M.; Brooks, R. A.; Baumgarner, C.; Vymazal, J.; Strub, M.-P.; Frank, J. A. Magnetoferritin: Characterization of a Novel Superparamagnetic MR Contrast Agent. *J. Magn. Reson. Imaging* **1994**, *4*, 497–505.

22. Gider, S.; Awschalom, D. D.; Douglas, T.; Mann, S.; Chaparala, M. Classical and Quantum Magnetic Phenomena in Natural and Artificial Ferritin Proteins. *Science* **1995**, *268*, 77–80.

23. Pankhurst, Q. A.; Betteridge, S.; Dickson, D. P. E.; Douglas, T.; Mann, S.; Frankel, R. B. Mössbauer Spectroscopic and Magnetic Studies of Magnetoferritin. *Hyperfine Interact.* **1994**, *91*, 847–851.

24. Kostiainen, M. A.; Ceci, P.; Fornara, M.; Hiekkataipale, P.; Kasyutich, O.; Nolte, R. J.; Cornelissen, J. J.; Desautels, R. D.; van Lierop, J. Hierarchical Self-Assembly and Optical Disassembly for Controlled Switching of Magnetoferritin Nanoparticle Magnetism. *ACS Nano* **2011**, *5*, 6394–6402.

25. Fittipaldi, M.; Innocenti, C.; Ceci, P.; Sangregorio, C.; Castelli, L.; Sorace, L.; Gatteschi, D. Looking for Quantum Effects in Magnetic Nanoparticles Using the Molecular Nanomagnet Approach. *Phys. Rev. B* **2011**, *83*, 104409.

26. Kostiainen, M. A.; Hiekkataipale, P.; Laiho, A.; Lemieux, V.; Seitsonen, J.; Ruokolainen, J.; Ceci, P. Electrostatic Assembly of Binary Nanoparticle Superlattices Using Protein Cages. *Nat. Nanotechnol.* **2013**, *8*, 52–56.

27. Allen, M.; Willits, D.; Young, M.; Douglas, T. Constrained Synthesis of Cobalt Oxide Nanomaterials in the 12-Subunit Protein Cage from Listeria Innocua. *Inorg. Chem.* **2003**, *42*, 6300–6305.

28. Resnick, D. A.; Gilmore, K.; Idzerda, Y. U.; Klem, M. T.; Allen, M.; Douglas, T.; Young, M.; Arenholz, E. Magnetic Properties of Co_3O_4 Nanoparticles Mineralized in Listeria Innocua Dps. *J. Appl. Phys.* **2006**, *99*, 08Q501.

29. Mackle, P.; Charnock, J. M.; Garner, C. D.; Meldrum, F. C.; Mann, S. Characterization of the Manganese Core of Reconstituted Ferritin by X-Ray Absorption Spectroscopy. *J. Am. Chem. Soc.* **1993**, *115*, 8471–8472.

30. Warne, B.; Kasyutich, O.; Mayes, E. L.; Wiggins, J. A. L.; Wong, K. K. W. Self Assembled Nanoparticulate Co: Pt for Data Storage Applications. *IEEE Trans. Magn.* **2000**, *36*, 3009–3011.

31. Ueno, T.; Suzuki, M.; Goto, T.; Matsumoto, T.; Nagayama, K.; Watanabe, Y. Size-Selective Olefin Hydrogenation by a Pd Nanocluster Provided in an Apo-Ferritin Cage. *Angew. Chem., Int. Ed.* **2004**, *43*, 2527–2530.

32. Kramer, R. M.; Li, C.; Carter, D. C.; Stone, M. O.; Naik, R. R. Engineered Protein Cages for Nanomaterial Synthesis. *J. Am. Chem. Soc.* **2004**, *126*, 13282–13286.

33. Wong, K. K. W.; Mann, S. Biomimetic Synthesis of Cadmium Sulfide-Ferritin Nanocomposites. *Adv. Mater.* **1996**, *8*, 928–932.

34. Yamashita, I.; Hayashi, J.; Hara, M. Bio-Template Synthesis of Uniform CdSe Nanoparticles Using Cage-Shaped Protein, Apoferritin. *Chem. Lett.* **2004**, *33*, 1158–1159.

35. Iwahori, K.; Yoshizawa, K.; Muraoka, M.; Yamashita, I. Fabrication of ZnSe Nanoparticles in the Apoferritin Cavity by Designing a Slow Chemical Reaction System. *Inorg. Chem.* **2005**, *44*, 6393–6400.

36. Fortin, J.-P.; Wilhelm, C.; Servais, J.; Ménager, C.; Bacri, J.-C.; Gazeau, F. Size-Sorted Anionic Iron Oxide Nanomagnets as Colloidal Mediators for Magnetic Hyperthermia. *J. Am. Chem. Soc.* **2007**, *129*, 2628–2635.

37. Gonzales-Weimuller, M.; Zeisberger, M.; Krishnan, K. Size-Dependent Heating Rates of Iron Oxide Nanoparticles for Magnetic Fluid Hyperthermia. *J. Magn. Magn. Mater.* **2009**, *321*, 1947–1950.

38. Purushotham, S.; Ramanujan, R. V. Modeling the Performance of Magnetic Nanoparticles in Multimodal Cancer Therapy. *J. Appl. Phys.* **2010**, *107*, 114701.

39. Lartigue, L.; Innocenti, C.; Kalaivani, T.; Awwad, A.; del Mar Sanchez Duque, M.; Guari, Y.; Larionova, J.; Guérin, C.; Montero, J.-L. G.; Barragan-Montero, V.; *et al*. Water-Dispersible Sugar-Coated Iron Oxide Nanoparticles. An Evaluation of Their Relaxometric and Magnetic Hyperthermia Properties. *J. Am. Chem. Soc.* **2011**, *133*, 10459–10472.

40. Comes Franchini, M.; Baldi, G.; Bonacchi, G.; Gentili, D.; Giudetti, G.; Lascialfari, A.; Corti, M.; Marmorato, P.; Ponti, J.; Micotti, E.; *et al*. Bovine Serum Albumin-Based Magnetic Nanocarrier for MRI Diagnosis and Hyperthermic Therapy: A Potential Theranostic Approach Against Cancer. *Small* **2010**, *6*, 366–370.

41. Fantechi, E.; Campo, G.; Carta, D.; Corrias, A.; de Julián Fernandez, C.; Gatteschi, D.; Innocenti, C.; Rugi, F.; Sangregorio, C. Exploring the Effect of Co Doping in Fine Maghemite Nanoparticles. *J. Phys. Chem. C* **2012**, *116*, 8261–8270.

42. Miao, Y.; Quinn, T. P. Peptide-Targeted Radionuclide Therapy for Melanoma. *Crit. Rev. Oncol. Hematol.* **2008**, *67*, 213–228.

43. Vannucci, L.; Falvo, E.; Fornara, M.; Di Micco, P.; Benada, O.; Krizan, J.; Svoboda, J.; Hulikova-Capkova, K.; Morea, V.; Boffi, A.; *et al*. Selective Targeting of Melanoma by PEG-Masked Protein-Based Multifunctional Nanoparticles. *Int. J. Nanomed.* **2012**, *7*, 1489–1509.

44. Vannucci, L.; Falvo, E.; Failla, M. C.; Carbo, M.; Fornara, M.; Canese, R.; Cecchetti, S.; Rajsiglova, L.; Stakheev, D.; Krizan, J.; *et al*. In Vivo Targeting of Cutaneous Melanoma Using an MSH-Engineered Human Protein Cage with Fluorophore and MRI Tracers. *J. Biomed. Nanotechnol.* **2014**, DOI: 10.1166/jbn.2014.1946.

45. Verbeeck, J.; Van Aert, S. Model Based Quantification of EELS Spectra. *Ultramicroscopy* **2004**, *101*, 207–224.

46. Bencini, A.; Gatteschi, D. ESR Spectra of Metal Complexes of the First Transition Series in Low-Symmetry Environments. *Transition Met. Chem.* **1982**, *8*, 1–178.

47. Hergt, R.; Dutz, S. Magnetic Particle Hyperthermia—Biophysical Limitations of a Visionary Tumor Therapy. *J. Magn. Magn. Mater.* **2007**, *311*, 187–192.

48. Lascialfari, A.; Filibian, V.; Sangregorio, C.; Carretta, P. In Vivo Biomedical Applications of Magnetic Resonance and Magnetic Materials. *Riv. Nuovo Cimento Soc. Ital. Fis.* **2013**, *6*, 211–271.

49. Guardia, P.; Di Corato, R.; Lartigue, L.; Wilhelm, C.; Espinosa, A.; Garcia-Hernandez, M.; Gazeau, F.; Manna, L.; Pellegrino, T. Water-Soluble Iron Oxide Nanocubes with High Values of Specific Absorption Rate for Cancer Cell Hyperthermia Treatment. *ACS Nano* **2012**, *6*, 3080–3091.

50. Lee, J.-H.; Jang, J.-T.; Choi, J.-S.; Moon, S. H.; Noh, S.-H.; Kim, J.-W.; Kim, J.-G.; Kim, I.-S.; Park, K. I.; Cheon, J. Exchange-Coupled Magnetic Nanoparticles for Efficient Heat Induction. *Nat. Nanotechnol.* **2011**, *6*, 418–422.

51. Néel, L. Théorie du Traînage Magnétique des Ferromagnétiques en Grains Fins avec Applications aux Terres Cuites. *Ann. Geophys.* **1949**, *5*, 99–136.

52. Cannas, C.; Concas, G.; Gatteschi, D.; Falqui, A.; Musinu, A.; Piccaluga, G.; Sangregorio, C.; Spano, G. Superparamagnetic Behaviour of γ-Fe$_2$O$_3$ Nanoparticles Dispersed in a Silica Matrix. *Phys. Chem. Chem. Phys.* **2001**, *3*, 832–838.

53. Batlle, X.; Pérez, N.; Guardia, P.; Iglesias, O.; Labarta, A.; Bartolomé, F.; García, L. M.; Bartolomé, J.; Roca, A. G.; Morales, M. P.; *et al.* Magnetic Nanoparticles with Bulk Like Properties. *J. Appl. Phys.* **2011**, *109*, 07B524.

54. Demortière, A.; Panissod, P.; Pichon, B. P.; Pourroy, G.; Guillon, D.; Donnio, B.; Bégin-Colin, S. Size-Dependent Properties of Magnetic Iron Oxide Nanocrystals. *Nanoscale* **2011**, *3*, 225–232.

55. Dormann, J. L.; Fiorani, D.; Tronc, E. Magnetic Relaxation in Fine-Particle Systems. *Adv. Chem. Phys.* **1997**, *98*, 283–494.

56. Klem, M. T.; Resnick, D. A.; Gilmore, K.; Young, M.; Idzerda, Y. U.; Douglas, T. Synthetic Control over Magnetic Moment and Exchange Bias in All-Oxide Materials Encapsulated within a Spherical Protein Cage. *J. Am. Chem. Soc.* **2007**, *129*, 197–201.

57. Kavich, D. W.; Dickerson, J. H.; Mahajan, S. V.; Hasan, S. A.; Park, J.-H. Exchange Bias of Singly Inverted FeO/Fe$_3$O$_4$ Core-Shell Nanocrystals. *Phys. Rev. B* **2008**, *78*, 174414.

58. Giri, S.; Patra, M.; Majumdar, S. Exchange Bias Effect in Alloys and Compounds. *J. Phys.: Condens. Matter* **2011**, *23*, No. 073201.

59. Nogués, J.; Sort, J.; Langlais, V.; Skumryev, V.; Suriñach, S.; Muñoz, J. S.; Baró, M. D. Exchange Bias in Nanostructures. *Phys. Rep.* **2005**, *422*, 65–117.

60. Nicholson, D. W.; Thornberry, N. A. Apoptosis. Life and Death Decisions. *Science* **2003**, *299*, 214–215.

61. Woo, M.; Hakem, R.; Soengas, M. S.; Duncan, G. S.; Shahinian, A.; Kägi, D.; Hakem, A.; Mc Currach, M.; Khoo, W.; Kaufman, S. A.; *et al.* Essential Contribution of Caspase 3/CPP32 to Apoptosis and its Associated Nuclear Changes. *Genes Dev.* **1998**, *12*, 806–819.

62. Kamada, S.; Kikkawa, U.; Tsujimoto, Y.; Hunter, T. Nuclear Translocation of Caspase-3 is Dependent on its Proteolytic Activation and Recognition of a Substrate-Like Protein(s). *J. Biol. Chem.* **2005**, *280*, 857–60.

63. Issels, R. Hyperthermia Combined with Chemotherapy-Biological Rationale, Clinical Application, and Treatment Results. *Onkologie* **1999**, *22*, 374–381.

64. Rosensweig, R. E. Heating Magnetic Fluid with Alternating Magnetic Field. *J. Magn. Magn. Mater.* **2002**, *252*, 370–374.

65. Riedinger, A.; Guardia, P.; Curcio, A.; Garcia, M. A.; Cingolani, R.; Manna, L.; Pellegrino, T. Subnanometer Local Temperature Probing and Remotely Controlled Drug Release Based on Azo-Functionalized Iron Oxide Nanoparticles. *Nano Lett.* **2013**, *13*, 2399–2406.

66. Villanueva, A.; de la Presa, P.; Alonso, J. M.; Rueda, T.; Martínez, A.; Crespo, P.; Morales, M. P.; Gonzalez-Fernandez, M. A.; Valdés, J.; Rivero, G. Hyperthermia HeLa Cell Treatment with Silica-Coated Manganese Oxide Nanoparticles. *J. Phys. Chem. C* **2010**, *114*, 1976–1981.

67. Egerton, R. F. *Electron Energy-Loss Spectroscopy in the Electron Microscope*; Plenum Press: New York, 1986.

68. Veerbeck, J.; Van Aert, S.; Bertoni, G. Model-Based Quantification of EELS Spectra: Including the Fine Structure. *Ultramicroscopy* **2006**, *106*, 976–980.

69. Schieber, M. M. Iron Oxides and Their Compounds. In *Experimental Magnetochemistry: Nonmetallic Magnetic Materials*; Wohlfarth, E. P., Ed.; North-Holland Publishing Company: Amsterdam, 1967; pp 158 and 182.